Materials Advances

Accepted Manuscript

This article can be cited before page numbers have been issued, to do this please use: M. Brown, S. Borbon Rojas, L. Fernandez Izquierdo, R. Haroldson and M. A. Quevedo-López, *Mater. Adv.*, 2026, DOI: 10.1039/D6MA00161K.

ROYAL SOCIETY OF CHEMISTRY

rsc.li/materials-advances

View Article Online
DOI: 10.1039/D6MA00161K

Optimized Grain Growth in $CsPbBr_3$ Thick Films Using Mist-Assisted Dissolution-Recrystallization for Enhanced Optoelectronic Performance

Received 00th January 20xx,
Accepted 00th January 20xx

DOI: 10.1039/x0xx00000x

Monet Brown, [a] Susana Borbon-Rojas, [a] Leunam Fernandez-Izquierdo, [a] Ross Haroldson [a] and Manuel Quevedo-Lopez*[a]

All-inorganic metal halide perovskite (MHP) thick films offer exceptional promise for photodetector applications (visible, UV, X-ray and gamma-ray) due to the stability of inorganic compositions and enhanced radiation absorption of thick-film architectures. However, their performance is often limited, compared to their single crystal counterparts, due to small grain sizes and high grain boundary densities which introduce trap states that reduce device efficiency. Here, we introduce a mist-assisted dissolution–recrystallization (MADR) process to enhance the microstructure of blade-coated $CsPbBr_3$ thick films (~200 µm). Applying a $CsPbBr_3$/DMSO mist at controlled concentrations (0.1–0.4 M) followed by low-temperature annealing (60–110 °C) drives a 3.8-fold increase in average grain size from 0.83 ± 0.28 to 3.19 ± 1.57 µm. Under optimal conditions (0.1 M mist, 85 °C anneal), the MADR-treated film exhibits enlarged grains, reduced trap density, and improved crystallinity, resulting in a ~10^3 order photocurrent enhancement from 1.02 × 10^{-7} to 4.5 × 10^{-4} A/cm² at 5 V under 365 nm illumination (125 mW/cm²). This MADR approach on blade coated films provides scalable, high-quality perovskite films with low thermal budget and broad substrate compatibility, offering a versatile route for radiation detection and optoelectronic devices.

Introduction

The exceptional properties of $CsPbBr_3$ such as a wide bandgap (□2.3 eV), high atomic numbers (Cs = 55, Pb = 82, and Br = 35), and large mobility-lifetime product of (3.2 × 10-3 cm²/V) have driven substantial interest in optoelectronic applications including sensors, lasers, and photovoltaics.[1–3] The wide band gap reduces dark current, improving the signal-to-noise ratio, while the high atomic numbers increase the photoelectric absorption.[2,4] These properties have enabled perovskite X-ray detectors to achieve ~200-fold higher sensitivity and ~100-fold lower detection limits than conventional a-Se-based X-ray detectors.[4,5] However, these results are primarily achieved in single crystals of $CsPbBr_3$, which are challenging to scale for commercial manufacturing.[4,6] While scalable methods exist for perovskite thin films (<1 µm), clinically relevant X-ray energies (10 to 100 keV) require 100 to 500 µm thickness for full attenuation.[4,7–9] Similarly, exceptional performance has been reported for visible-UV photodetectors. Bin Yang et al. reported solution grown polycrystalline $CsPbBr_3$ thick films with detectivities of 10^{14} Jones, exceeding single crystals having a reported detectivity of 10^{11} Jones under U-V exposure.[10,11] However, solution submersion methods are incompatible with many device architectures.[4] Blade coating has emerged as a scalable fabrication method for perovskite thick films; however, achieving high material quality with controlled grain size remains a critical challenge.[4,12–14]

Kim et al. report that the mobility-lifetime product (µτ) of the $MAPbI_3$ blade-coated thick film (1.0 × 10^{-4} cm² V^{-1}) is two orders of magnitude lower than that of single-crystal $MAPbI_3$ (1.2 × 10-² cm² V^{-1}), highlighting the need to improve performance in blade-coated films.[15,16] Cheng et al. addressed this need in $MAPbI_3$ blade-coated thick films using a pore-filling method that enhanced X-ray sensitivity 5-fold, from 323.86 to 1616.01 µC·$Gyair^{-1}$ cm^{-2} under an electric field of 44.44 V·mm^{-1}.[6] While this approach has advanced hybrid perovskite thick films, all inorganic perovskite films remain essential for applications requiring long term operational stability in ambient environments.[17,18] For all-inorganic systems such as $CsPbBr_3$, Shi et al. and Gou et al. employed dissolution-recrystallization to improve material quality and increase sensitivity via a powder "washing" pre-deposition treatment and a surface treatment, respectively.[17,19] These approaches increased the sensitivity from 798 to 14,430 µC·$mGyair^{-1}$·cm^{-2} at 100 V·mm^{-1} (Shi et al.) and the methods reported by Gou et al. resulted in a 2-fold sensitivity increase.[17,19] Building on these strategies, this work introduces a novel mist-assisted dissolution-recrystallization technique to increase bulk grain size and crystallite size in all-inorganic perovskite thick films (~200 µm).

Leveraging crystallization kinetics to control grain coarsening and crystallite size in blade-coated $CsPbBr_3$ thick films, this work systematically decouples the processing conditions that govern dissolution-recrystallization dynamics, establishing a framework for enhancing film quality and device-relevant optoelectronic properties at low processing temperatures. Grain size refers to the dimensions of individual particles observed by microscopy, whereas crystallite size represents the coherent scattering domain size determined from XRD analysis. This method employs a DMSO-based mist solution containing dissolved $CsPbBr_3$ (0.1 M, 0.2 M, or 0.4 M) applied to blade-coated $CsPbBr_3$ thick films. The mist penetrates the bulk of the film and partially dissolves the perovskite, creating a saturated or supersaturated environment. Upon annealing at controlled temperatures (60, 85, or 110 °C), the system undergoes Ostwald

[a] Department of Material Science & Engineering, University of Texas at Dallas,2601 N. Floyd Rd. RL10 Richardson, TX. 75080

† The data supporting this article have been included as part of the Supplementary Information. Supplementary information: Figure S1, Tables S1, Figure S2, Figure S3, Table S2 and Figure S4 and further experimental details. See DOI: [URL – format https://doi.org/DOI]

ripening withing the metastable zone, where grain coarsening, distinct from nucleation and crystal growth, proceeds via surface-energy-driven material transport from smaller grains to larger grains.[20,21] This mist-assisted dissolution-recrystallization (MADR) technique achieves substantial grain size increases with optimal conditions (0.1 M, 85 °C) yielding grain sizes of 3.19 ± 1.57 µm compared to 0.83 ± 0.28 µm in the as-deposited films. Correspondingly, photocurrent response, a key metric for evaluating charge collection efficiency in photodetector applications, increases by over three orders of magnitude, from 1.02×10^{-7} to 4.5×10^{-4} A/cm^2 at 5 V in a Pt/$CsPbBr_3$/Pt planar device illuminated with a 365 nm LED at 125 mW/cm^2. These results demonstrate that controlled temperature-concentration dynamics enable targeted grain coarsening in $CsPbBr_3$, substantially improving optoelectronic performance. This solution-based approach is generalizable to diverse perovskite systems and can be applied iteratively to multiply performance enhancements, offering a scalable pathway toward high-efficiency thick film perovskite optoelectronic devices and radiation detectors.

Results

While $CsPbBr_3$ single-crystals and thin films have been reported to exhibit excellent optoelectronic properties, thick-films (100-500 µm) required for commercially relevant high energy photon applications often struggle to achieve large grains, high crystallinity, and high carrier mobility[4]. Overcoming these processing challenges is therefore essential for translating the intrinsic properties of MHPs into practical device performance. **Figure 1(a) and (b)** show cross-section SEM images of the as-deposited $CsPbBr_3$ thick film fabricated by blade coating. The as-deposited film exhibits a highly porous microstructure with small grains, characteristic of blade-coated films.[4,13] **Figure 1(c)** shows the grain size distribution of the as-deposited $CsPbBr_3$ film, with an average grain size of 0.83 ± 0.28 µm. Such a small

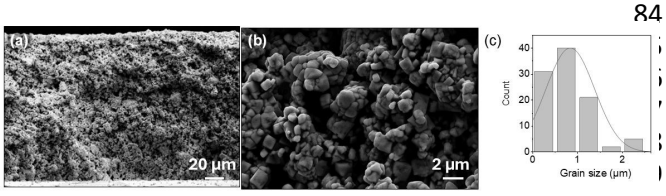

Figure 1: (a) and (b): SEM cross section of as-deposited $CsPbBr_3$ 200 µm thick film. (c) Grain size distribution of the as-deposited $CsPbBr_3$ 200 µm thick film. The average grain size of 50 grains is 0.83 ± 0.28 µm.

grain-to-thickness ratio and high porosity commonly leads to reduced device performance.[4,19] Subsequently, MADR treatment was applied to improve film quality. We systematically investigated the effects of annealing temperature and mist concentration on grain morphology and crystallite size. The DMSO/$CsPbBr_3$ mist induces partial dissolution when applied to the porous, fine-grained as-deposited film and subsequent annealing promotes grain growth that increases film density, grain size, and crystallite size.

Impact of Mist Concentration and Annealing Temperature on $CsPbBr_3$ Film Microstructure.

To promote grain growth, MADR was performed on as-deposited $CsPbBr_3$ thick films. Exposure to pure DMSO mist caused nonuniform grain size distribution (**Figure S1**), whereas incorporating $CsPbBr_3$ into the mist enabled more homogeneous solvent-film interactions and improved film uniformity. A DMSO/$CsPbBr_3$ mist solution was applied at concentrations of 0.1 M, 0.2 M, and 0.4 M due to the solubility limit of $CsPbBr_3$ in DMSO (0.5 M).[22] Cross-sectional SEM images of films treated at each mist concentration are shown in **Figure 2**. Low mist concentration (0.1 M) produced larger grains (1.91-3.19 µm), attributed to more uncoordinated DMSO molecules that promote Ostwald ripening.[20,21] Conversely, at higher mist concentrations (0.4 M) there is limited dissolution, yielding smaller grains (0.97-1.52 µm).[11,23–25] Recrystallization temperatures of 60, 85, and 110 °C were selected to probe solvent assisted growth kinetics below the 189 °C boiling point of DMSO (**Figure 2**). Annealing at 85 °C produced the largest grain size increase (1.45 - 3.19 µm). At 60 °C, insufficient thermal energy limits grain coarsening (0.97-2.09 µm), whereas at 110 °C, faster DMSO evaporation suppresses further growth (1.52-1.91 µm). Grain sizes and corresponding standard deviations are summarized in **Table S1**.

These observations are consistent with established crystallization kinetics models: within the solubility and supersolubility boundaries (metastable zone), Ostwald ripening is the dominant mechanism; whereas above the supersolubility boundary (labile region), supersaturation promotes spontaneous crystallization and suppresses ripening.[20,21,23,24] Under optimal conditions, average grain size increased from 0.83 ± 0.28 µm in the as-deposited film to 3.19 ± 1.57 µm with 0.1 M mist and a 85 °C anneal, indicating that this condition lies near the center of the metastable zone where ripening is most pronounced.[23,26] These parameters collectively define useful boundaries for distinguishing the metastable and labile regions. XRD analysis, discussed in the next section, was conducted to validate the proposed mechanism by quantifying crystallite size evolution. Larger crystallite sizes at higher mist concentrations corroborate the SEM results and crystallization kinetics described above.[23]

View Article Online
DOI: 10.1039/D6MA00161K

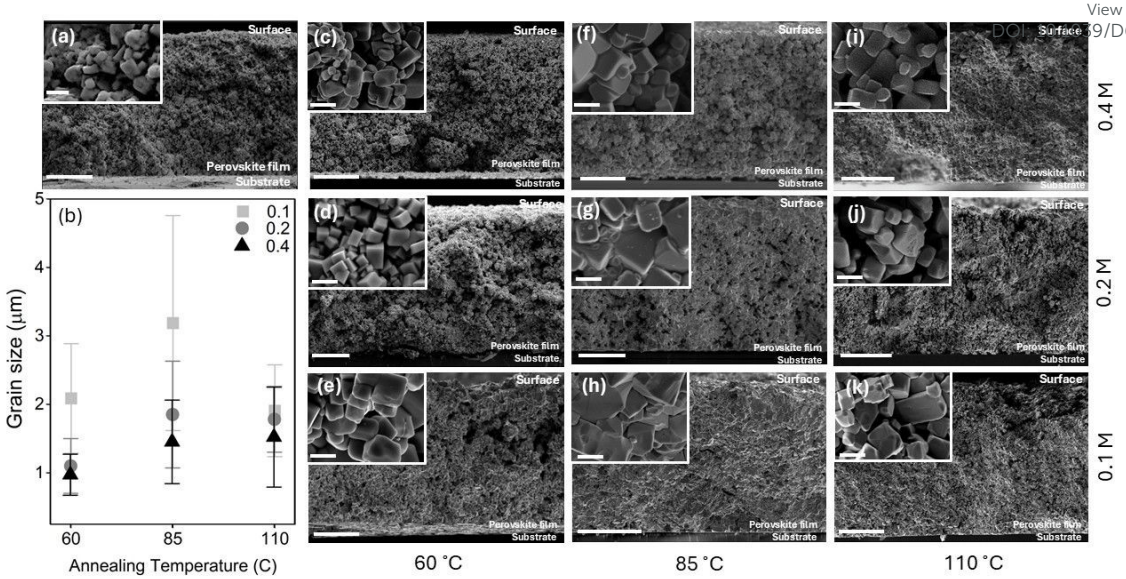

View Article Online
DOI: 10.1039/D6MA00161K

Figure 2: SEM cross sectional images of (a) as-deposited bladed-coated $CsPbBr_3$ film and (b) grain size distribution of mist-assisted dissolved and recrystallized $CsPbBr_3$ films. The films were annealed at (c-e) 60 °C, (f-h) 85 °C, and (i-k) 110 °C using a mist solution of DMSO and $CsPbBr_3$ powder at concentrations of 0.1 M (bottom row), 0.2 M (middle row), and 0.4 M (top row). All scale bars represent 50 µm and 2 µm in insets.

Impact of Mist Concentration and Annealing Temperature on $CsPbBr_3$ Crystallinity

The effects of mist solution concentration and annealing temperature on film composition were evaluated by X-ray diffraction (**Figure 3)**. At moderate mist concentration (0.2 M), secondary Cs-Pb-Br phases formed at 60°C, whereas higher mist concentration (0.4 M) induces secondary phase formation at both 60 and 85°C. At 60 °C, diffraction peaks at 11.6, 12.5, 30.9, and 32 2θ (Degrees) correspond to the tetragonal $CsPb_2Br_5$ and rhombohedral Cs_4PbBr_6 (**Figure S2**). Peaks associated with rhombohedral Cs_4PbBr_6 appeared in 0.4 M films annealed at 85 °C (**Figure S3**). No reflections associated with secondary phases were observed at 110 °C. Phase compositions are summarized in **Table S1**.

The XRD data were further analyzed to estimate crystallite size using the Scherrer equation.[27] As shown in **Figure 3(d),** MADR treatment at 85 °C with 0.1 M mist concentration increased crystallite size to 44.22 ± 10.81 nm from 40.92 ± 2.66 nm in the as-deposited film. At 110 °C with 0.4 M mist concentration, the crystallite size increased to 125.48 ± 9.56 nm, the maximum observed value. Crystal growth occurs via the expansion of a single crystalline domain through coalescence of domains with coherent planes, a process favored by the high supersaturation conditions that bring crystallites into proximity.[28] Grain growth results from the aggregation of multiple domains with incoherent planes. Correlation of XRD and SEM results show that variations in mist concentration and annealing temperature modulate the balance between these mechanisms, determining which mechanism dominates under specific MADR conditions.

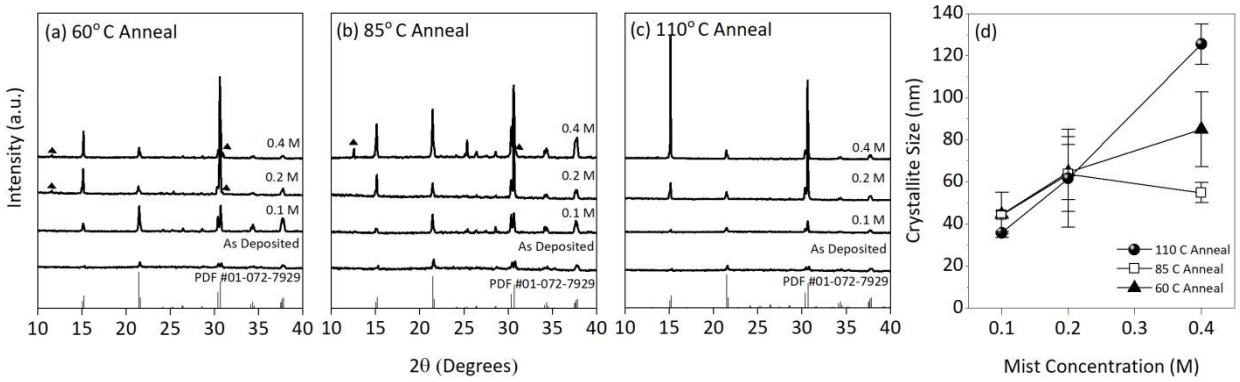

Figure 3: X-ray diffraction patterns for the as-deposited and treated films at each mist solution concentration (0.1, 0.2 and 0.4 M) and annealed at (a) 60 °C, (b) 85 °C, (c) 110 °C are presented. Peaks that do not correspond to Orthorhombic $CsPbBr_3$ are accompanied by a triangle with tetragonal $CsPb_2Br_5$ and rhombohedral Cs_4PbBr_6 present at 60 °C and rhombohedral Cs_4PbBr_6 at 85 °C. (d) Crystallite size as a function of concentration and mist solution concentration.

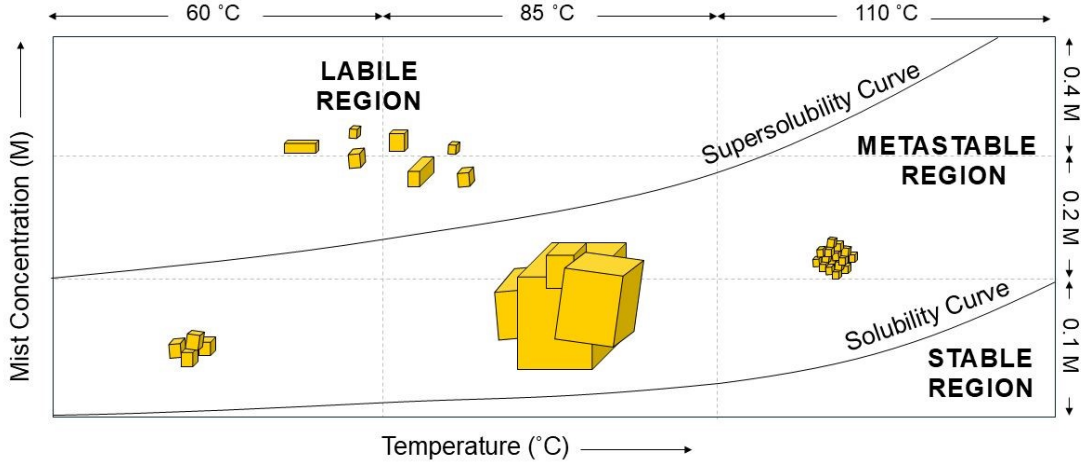

Figure 4: Schematic showing grain growth and crystal growth as a function of mist concentration and annealing temperature in $CsPbBr_3$ films as an adaptation of classic crystallization models.[23,24] Optimal grain growth occurs at moderate temperature (85 °C) and low concentration (0.1 M) within the metastable region. Higher concentrations promotes rapid crystallization, yielding smaller grains with larger crystallite sizes.

View Article Online
DOI: 10.1039/D6MA00161K

The combined SEM and XRD results are interpreted within a thermodynamic-kinetic model for crystallization. At low mA concentrations, the system lies within the metastable region, where abundant uncoordinated DMSO molecules promote grain coarsening through Ostwald ripening, resulting in larger grain sizes but minimal change in crystallite size.[21,23,26] Increasing mA concentration shifts the system toward the labile region, where reduced DMSO availability limits solvent-induced ripening, and unstable supersaturation promotes spontaneous crystallization, producing smaller grains with larger crystallite size.[21,23,26] Annealing temperature further modulates these effects as DMSO, with a boiling point of 189 °C, exhibits slow evaporation kinetics at 60 °C that progressively increase up to 110 °C. Therefore, SEM grain size peaks at moderate temperature 85 °C where thermal energy is sufficient for grain coarsening, while XRD crystallite size increases with temperature as faster solvent evaporation at 110 °C favors crystalline ordering and lacks the solvent availability for grain growth (**Figure S4**). The resulting microstructure is therefore governed by the coupled effects of supersaturation and temperature, as illustrated in **Figure 4.**

Figure 5: (a) Photoluminescence Spectroscopy of the as-deposited film and recrystallized film saturated with a 0.1 M solution and annealed at 85 °C. Figures (b -c) show the fitting of the PL spectra.

Impact of Grain Growth and Crystallite Size on Optoelectronic Properties

The recrystallized film with the largest grains and lowest porosity (0.1 M, 85 °C) was selected, as grain boundaries and pores act as primary barriers to charge transport in polycrystalline films.[16,29] This film was compared to the as deposited film and evaluated using steady-state photoluminescence (PL). As shown in **Figure 5**, two emission bands appear: a primary $CsPbBr_3$ band at 525 nm and a secondary band near 540 nm, attributed to defect-related emission in $CsPbBr_3$.[10] Band-fitting results are shown in **Figures 5(b) and (c)**. The PL spectra were fitted with a mixed Gaussian-Lorentzian function in OriginPro 2025, yielding reduced chi-squared values <1 x 10^{-5} (see **Table S2**). The recrystallized film exhibits reduced relative intensity in the 540 nm defect-related band and enhanced emission at 525 nm, indicating that MADR treatment significantly reduces defect states. Furthermore, the PL emission of the 0.2 M film deposited at 60 °C, which contains secondary phases ($CsPb_2Br_5$ and Cs_4PbBr_6) as identified by XRD, is blue-shifted relative to the 0.2 M films deposited at 85 °C and 110 °C, which consist of phase-pure $CsPbBr_3$, consistent with prior reports of blue-shifted emission in Cs-Pb-Br systems containing Cs_4PbBr_6 secondary phases (see **Figure S5**).[30]

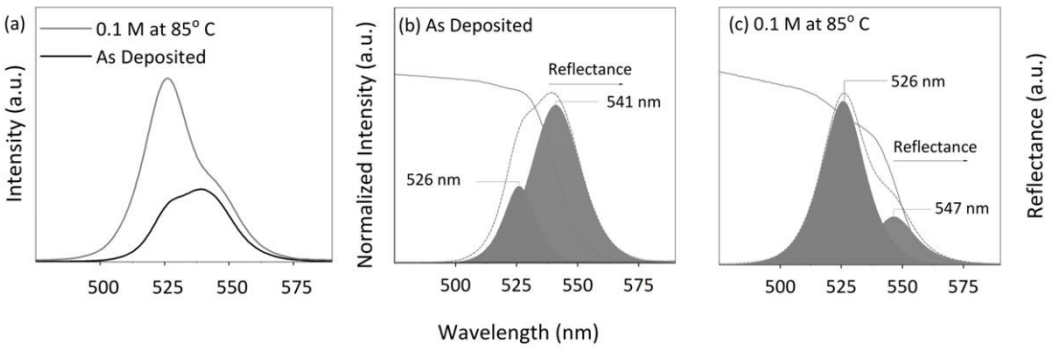

View Article Online
DOI: 10.1039/D6MA00161K

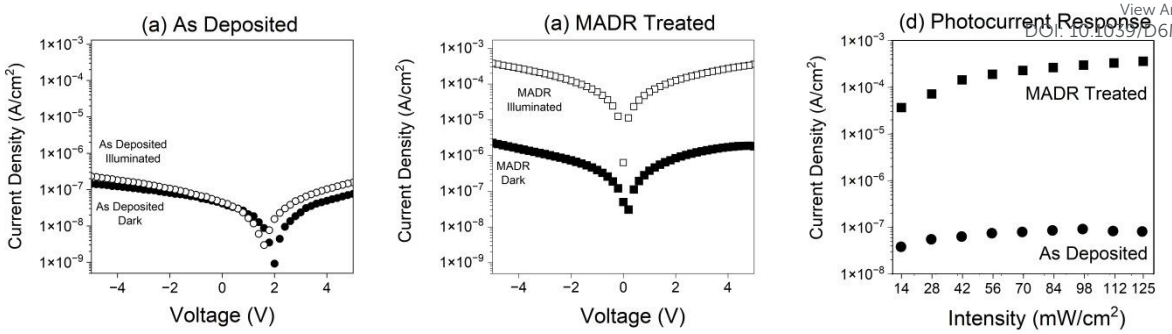

Figure 6: IV characterization of (a) the as-deposited film compared to (b) the film recrystallized with a 0.1 M solution at 85°C under dark conditions and illuminated at 125 mW/cm² and (c) photocurrent response of the as-deposited film and the recrystallized film across illumination intensities at 5 V.

The photocurrent response for the planar Pt/$CsPbBr_3$/Pt devices fabricated from the as-deposited film and selected recrystallized film was evaluated using a 365 nm light source (from dark to 125 mW/cm², (**Figure 6a-b**). The recrystallized film shows higher photocurrent, consistent with reduced defect density from steady state PL. MADR-induced grain coarsening reduces grain boundary density and passivates trap states, eliminating the asymmetry observed in the as-deposited film.[31,32] **Figure 6c** shows the photocurrent response at 5 V as a function of illumination intensity. At 5 V bias, the as deposited film exhibits 1.02×10^{-7} A/cm², whereas the recrystallized film shows a 4400-fold enhancement to 4.5×10^{-4} A/cm² (**Figure 5c**). The sheet conductance of the as-deposited film was determined to be 1.44×10^{-11} S, increasing to 2.72×10^{-10} S following MADR treatment, indirectly indicating enhanced charge transport in the recrystallized film (see **Section S2**).

Current-time measurements under a 125 mW cm⁻² illumination intensity results in a photocurrent response of 9.3×10^{-8} A/cm² for the as-deposited film, while the recrystallized film reaches 3.8×10^{-4} A/cm². The recrystallized film also exhibits rise and decay times of <27.4 ms and <4.6 ms respectively (**Figure 7a-b)**. As shown in **Figure 7(c) and (d)**, both photocurrent and response speed improve with increasing illumination intensity (f2.2 to 125 mW/cm²). Higher light intensity generates more electron-hole pairs and progressively fills trap states, reducing the density of available trapping sites that would otherwise delay charge collection.[33]

The as-deposited film exhibited a responsivity of 1.07×10^{-5} A/W and a specific detectivity of 3.58×10^{6} Jones. Following MADR treatment, the responsivity and detectivity increased to 3.59×10^{-3} A/W and 5.04×10^{9} Jones, respectively, demonstrating a significant enhancement in photodetector performance upon recrystallization (see **Section S3**). To assess ambient stability, the MADR treated film was stored unencapsulated between 20–30 °C and 45–65% RH for 6 months, after which it retained a sustained photocurrent response exceeding 10 continuous minutes, demonstrating reasonable long-term operational stability (see **Figure S6**).

Hot-pressed $CsPbBr_3$ pellets fabricated from mechanochemically synthesized ball-milled powder exhibit a comparable grain size (~0.35 µm, converted from the reported grain area) and a higher absolute photocurrent response (~10^{-7} A) relative to the as-deposited film in this work (0.83 ± 0.28 µm and 9×10^{-11} A).[3] MADR treatment induces a pronounced increase in photocurrent from the low response of the as deposited film (9×10^{-11} A, corresponding to 1.02×10^{-7} A/cm²) to a photocurrent density of 4.5×10^{-4} A/cm² under identical measurement conditions. Solution-grown polycrystalline films, such as those reported by Yang et al., show higher photocurrent densities (1.2×10^{-2} A/cm², calculated from the reported data), indicating the upper performance limits achievable with highly crystalline thick films.[10]

Figure 7: Time-current response of (a) the as-deposited film and (b) the film recrystallized with a 0.1 M solution at 85˚C. (c) The time-current response of the recrystallized film was measured with logarithmically spaced illumination intensity from 0.03 mW/cm2 to 125

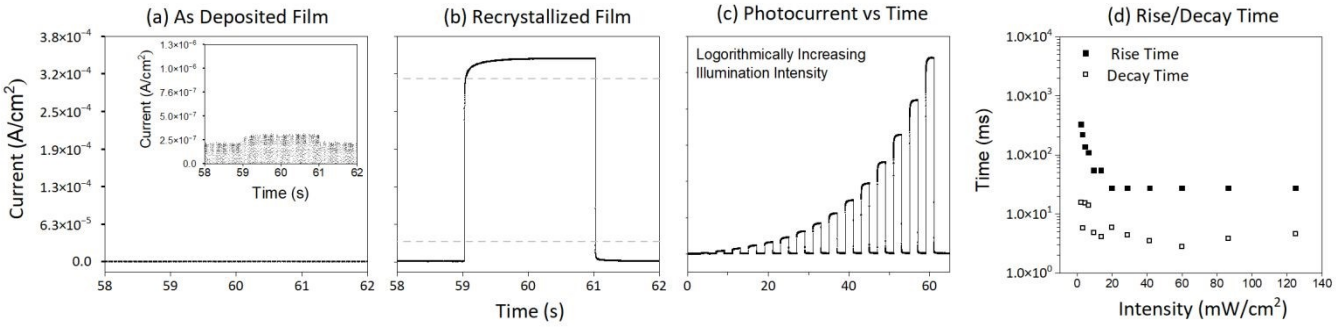

mW/cm². (d) Rise and decay times of the recrystallized sample across logarithmically spaced illumination intensities from 2.2 mW/cm² to 125 mW/cm². Measurements were made under 5 V bias with a 365 nm light source.

View Article Online
DOI: 10.1039/D6MA00161K

Table 1: $CsPbBr_3$ thick films are compared by fabrication method and their properties (grain size, thickness, processing temperature, and photocurrent response).

Fabrication Method	Average Grain Size (µm)	Thickness (µm)	Processing Temperature (˚C)	Photocurrent (A)	Photocurrent Density (A/cm²)	Ref.
Mechanochemical and Hot Pressing	0.35	400-700	100	$\sim 10^{-8}$	-	3
Blade Coated	0.83 ± 0.28	~ 200	85	1.02×10^{-11}	1.02×10^{-7}	This work
Dissolution-Recrystallization	3.19 ± 1.57	~ 200	85	3.75×10^{-7}	4.5×10^{-4}	This work
Solution Grown Microcrystals	-	~ 200	140	6.0×10^{-3}	1.2×10^{-2}	10

MADR-treated blade-coated films nonetheless exhibit competitive photocurrent response, with further improvements anticipated through iterative dissolution-recrystallization cycles. When considered alongside scalability, low thermal budget, and broad substrate compatibility, this approach represents a feasible route to large-scale perovskite thick film fabrication for optoelectronic applications. A comparison of these fabrication techniques are summarized in **Table 1**.

Experimental

The schematic of the MADR method for bulk recrystallization of blade-coated $CsPbBr_3$ films is shown in **Figure 8**. In this method, the CsBr and $PbBr_2$ precursors are ball-milled to synthesize the $CsPbBr_3$ powder. The $CsPbBr_3$ powder is then used to prepare a slurry to deposit a 200 µm thick film onto a glass substrate using a conventional Dr. Blade method. After film deposition, the $CsPbBr_3$ films are partially dissolved using a $CsPbBr_3$/DMSO mist solution at concentrations of 0.1, 0.2 and 0.4 M and then annealed at either 60, 85 or 110 ˚C for 30 minutes. Platinum contacts were used for the fabrication of the devices used for optoelectronic characterization.

Materials

Cesium bromide (CsBr, 99.9%) was obtained from Alfa-Aesar and Lead (II) bromide ($PbBr_2$, 99.99%) and dimethyl sulfoxide (DMSO) from Sigma-Aldrich. For the ball milling process, stainless-steel balls (2 mm), milling jars, and a high-energy vertical planetary ball mill were acquired from MSE Supplies LLC.

Blade Coated Film

Glass substrates underwent sequential 10-minute sonication steps in acetone, isopropyl alcohol, deionized water, and methanol. After drying with nitrogen, the substrates were annealed at 115 °C for 2 minutes and cleaned with oxygen-based reactive ion etching (RIE) for 10 minutes to remove organic residues and moisture. $CsPbBr_3$ films were then deposited on the glass by blade coating. The $CsPbBr_3$ powder precursors were synthesized via mechanochemical ball milling following a previously reported method.[34] The resulting $CsPbBr_3$ powder was sieved through a 0.2 µm pore-sized mesh to prevent agglomerated particles in the blade coating slurry. To prepare the slurry for blade coating, 1.5 mg of ethyl cellulose was dissolved in a mixture of 0.3 mL of n-n dodecane and 0.7 mL of α-terpineol by sonicating for 20 minutes. The slurry is then prepared using 30 µL of the prepared solution per 100 mg of $CsPbBr_3$ ball milled

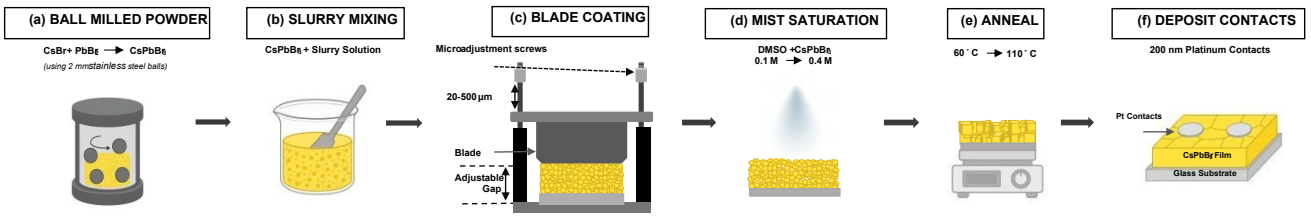

Figure 8. Experimental setup for: (a) ball milling of perovskite powder, (b) slurry preparation, (c) film deposition by blade coating, (d) film treatment with a mist solution, (e) annealing to facilitate recrystallization, and (f) deposition of Platinum contacts (E-beam evaporation).

powder. This slurry was then used to blade-coat $CsPbBr_3$ films onto a glass substrate at 2 mm/s at room temperature (Figure 8c). The blade coated films were annealed at 85 °C for 10 minutes with a heating ramp of 1 °C/min.

Mist-Assisted Dissolution-Recrystallization (MADR)

Next, the film was exposed to a mist solution for dissolution-recrystallization. The mist solution was prepared by dissolving ball-milled $CsPbBr_3$ powder in Dimethyl sulfoxide (DMSO) at 0.1, 0.2, and 0.4 M, followed by stirring for 18 hours at room temperature. Then 5 mL of the mist solution was applied to 200 µm thick films through a 0.5 mm nozzle propelled by nitrogen at 50 psi with a sample-to-nozzle distance of 15 inches, as shown in **Figure 1d**. Then annealed for 30 minutes at either 60, 85, or 110 ˚C using a ramp rate of 1 °C/min (**Figure 8e**).

Device Fabrication

Devices were fabricated by depositing platinum contacts (7×10^{-4} cm^2, 2×10^{-2} cm apart with an active area of 2×10^{-4} cm^2) onto the surface of $CsPbBr_3$ thick films via e-beam physical vapor deposition to fabricate a planar $Pt/CsPbBr_3/Pt$ architecture.

Material and Device Characterizations

Scanning electron microscopy (SEM) images of the polycrystalline blade coated thick films were obtained using a Zeiss Sigma 500VP. Cross-sectional images were acquired by cleaving the glass substrate supported films. The average grain size was measured using ImageJ software.[35] X-ray diffraction (XRD) patterns were obtained using a Rigaku SmartLab X-ray diffraction system equipped with a copper CuKα radiation source (λ = 1.5406 Å) at a current of 30 mA and voltage of 40 kV and crystallite size was calculated using the Scherer equation.[27] UV-Vis measurements were performed using an Agilent UV–Vis-NIR spectrophotometer with a Mercury arc lamp and multiangle reflection (R) capability. Steady state photoluminescence (PL) was measured with a 405 nm light emitting diode (LED), a 0.8 mm aperture, and an output of 100 mW/cm^2. Photocurrent response was measured using a 365 nm LED modulated from dark to 125 mW/cm^2. Current-Voltage characteristics of the planar $Pt/CsPbBr_3/Pt$ device were measured in a probe station with a Keithley 4200 system.

Conclusion

This study demonstrates a mist-assisted dissolution-recrystallization (MADR) process for scalable control of microstructure in blade-coated $CsPbBr_3$ thick films. At low mist concentrations, partial dissolution promotes grain coarsening through Ostwald ripening, yielding larger grains. Higher concentrations reduce dissolution, resulting in smaller grains. Annealing temperature modulates these effects: insufficient heating limits ripening, while excessive heating accelerates solvent evaporation and quenches grain growth. Careful control of mist concentration and annealing temperature enables precise grain and crystallite size tuning, significantly improving photo-response. This approach offers a pathway for engineering high-quality perovskite thick films for X-ray detection, photodetectors, and other applications requiring high-performance, large-area devices.

Author contributions

Monet Brown: Conceptualization, Data curation, Formal analysis, Investigation, Methodology, Visualization, Writing-origintal draft, Writing-review ad editing

Susana Borbon-Rojas: Methogology, Writing -review and editing

Leunam Fernandez-Izquierdo: Validation, Writing -review and editing

Ross Haroldson: Data curation

Manuel Quevedo-Lopez: Conceptualization, Funding acquisition, Project administration, Resources, Supervision, Validation, Writing-review and editing

Conflicts of interest

There are no conflicts to declare.

Data availability

The data supporting this article have been included as part of the Supplementary Information. Supplementary information: Figure S1, Tables S1, Figure S2, Figure S3, Table S2 and Figure S4 and further experimental details. See DOI: [URL – format https://doi.org/DOI]

Acknowledgements

The authors would like to express their gratitude to the University of Texas at Dallas and The Texas Instruments Chair in Nanoelectronics for partial financial support.

References

1 Y. Hua, X. Sun, X. Li, F. Cui, Z. Yue, J. Liu, H. Liu, G. Zhang and X. Tao, *J. Mater. Chem. C*, 2023, **11**, 9153–9160.

2 N. Grundmanis, A. Sarakovskis, A. Lupilov, V. Gostilo, A. Owens and K. Pudzs, *Nuclear Instruments and Methods in Physics Research Section A: Accelerators, Spectrometers, Detectors and Associated Equipment*, 2025, **1073**, 170305.

3 M. Sotelo-Lerma, L. Fernandez-Izquierdo, M. A. Ruiz-Molina, I. Borges-Doren, R. Haroldson and M. Quevedo-Lopez, *Materials*, DOI:10.3390/ma17205123.

4 Y. Haruta, M. Kawakami, Y. Nakano, S. Kundu, S. Wada, T. Ikenoue, M. Miyake, T. Hirato and M. I. Saidaminov, *Chem. Mater.*, 2022, **34**, 5323–5333.

5 J. Peng, C. Q. Xia, Y. Xu, R. Li, L. Cui, J. K. Clegg, L. M. Herz, M. B. Johnston and Q. Lin, *Nature Communications*, 2021, **12**, 1531.
6 J. Cheng, C. Xue, M. Yang, X. Wang, Z. Xu, N. Li, X. Zhang, X. Feng, X. Liu, Y. Liu, S. F. Liu and Z. Yang, *ACS Appl. Mater. Interfaces*, 2024, **16**, 36649–36657.
7 T. Zou, B. Xiang, Y. Xu, Y. Wang, C. Liu, J. Chen, K. Wang, Q. Dai, S. Zhang, Y. -Y. Noh, and H. Zhou, *IEEE Journal of the Electron Devices Society*, 2021, **9**, 96–101.
8 S. V. N. Pammi, V.-D. Tran, R. Maddaka, J.-H. Eom, J. S. Jung, H. M. Jeong, M.-D. Kim, V. Pecunia and S. G. Yoon, *Advanced Optical Materials*, 2020, **8**, 2000845.
9 S. V. N. Pammi, H.-W. Lee, J.-H. Eom and S.-G. Yoon, *ACS Appl. Energy Mater.*, 2018, **1**, 3301–3312.
10 B. Yang, F. Zhang, J. Chen, S. Yang, X. Xia, T. Pullerits, W. Deng and K. Han, *Advanced Materials*, 2017, **29**, 1703758.
11 Z. Zhang, H. Li, H. Di, D. Liu, W. Jiang, J. Ren, Z. Fan, F. Liao, L. Lei, G. Li, Y. Xiong and Y. Zhao, *ACS Appl. Electron. Mater.*, 2023, **5**, 388–396.
12 K.-W. Huang, M.-H. Li, Y.-T. Chen, Z.-X. Wen, C.-F. Lin and P. Chen, *J. Mater. Chem. C*, 2024, **12**, 1533–1542.
13 M. Xia, Z. Song, H. Wu, X. Du, X. He, J. Pang, H. Luo, L. Jin, G. Li, G. Niu and J. Tang, *Advanced Functional Materials*, 2022, **32**, 2110729.
14 B. Yang, W. Pan, H. Wu, G. Niu, J.-H. Yuan, K.-H. Xue, L. Yin, X. Du, X.-S. Miao, X. Yang, Q. Xie and J. Tang, *Nature Communications*, 2019, **10**, 1989.
15 H. Wei, Y. Fang, P. Mulligan, W. Chuirazzi, H.-H. Fang, C. Wang, B. R. Ecker, Y. Gao, M. A. Loi, L. Cao and J. Huang, *Nature Photonics*, 2016, **10**, 333–339.
16 Y. C. Kim, K. H. Kim, D.-Y. Son, D.-N. Jeong, J.-Y. Seo, Y. S. Choi, T. Han, S. Y. Lee and N.-G. Park, *Nature*, 2017, **550**, 87–91.
17 Z. Gou, S. Huanglong, W. Ke, H. Sun, H. Tian, X. Gao, X. Zhu, D. Yang and P. Wangyang, *physica status solidi (RRL) – Rapid Research Letters*, 2019, **13**, 1900094.
18 A. Choubey, N. Perumal, S. Narendhiran, S. P. Muthu and R. Perumalsamy, *International Journal of Energy Research*, 2022, **46**, 9310–9322.
19 T. Shi, W. Liu, J. Zhu, X. Fan, Z. Zhang, X. He, R. He, J. Wang, K. Chen, Y. Ge, X. Sun, Y. Liu, P. K. Chu and X.-F. Yu, *Nano Research*, 2023, **16**, 9983–9989.
20 X. Cao, L. Zhi, Y. Li, F. Fang, X. Cui, L. Ci, K. Ding and J. Wei, *ACS Appl. Energy Mater.*, 2018, **1**, 868–875.
21 T. Vetter, M. Iggland, D. R. Ochsenbein, F. S. Hänseler and M. Mazzotti, *Crystal Growth & Design*, 2013, **13**, 4890–4905.
22 X. Cao, G. Zhang, L. Hao, X. Ding, T. Dong, X. Li, Q. Zeng, X. He, Y. Jia and J. Wei, *Journal of Alloys and Compounds*, 2022, **919**, 165722.
23 Y. Zhang, in *Modelling of Chemical Process Systems*, ed. S. A. Imtiaz, Elsevier, 2023, pp. 181–202.
24 J.-P. Duroudier, in *Crystallization and Crystallizers*, ed. J.-P. Duroudier, Elsevier, 2016, pp. 39–78.
25 S. Kim and A. S. Myerson, *Ind. Eng. Chem. Res.*, 1996, **35**, 1078–1084.
26 M. A. Behrens, A. Franzén, S. Carlert, U. Skantze, L. Lindfors and U. Olsson, *Soft Matter*, 2025, **21**, 2349–2354.
27 P. Scherrer, *Math. Phys.*, 1918, **2**, 98–100.
28 S. Li, Y. Xiao, R. Su, W. Xu, D. Luo, P. Huang, L. Dai, P. Chen, P. Caprioglio, K. A. Elmestekawy, M. Dubajic, C. Chosy, J. Hu, I. Habib, A. Dasgupta, D. Guo, Y. Boeije, S. J. Zelewski, Z. Lu, T. Huang, Q. Li, J. Wang, H. Yan, H.-H. Chen, C. Li, B. A. I. Lewis, D. Wang, J. Wu, L. Zhao, B. Han, J. Wang, L. M. Herz, J. R. Durrant, K. S. Novoselov, Z.-H. Lu, Q. Gong, S. D. Stranks, H. J. Snaith and R. Zhu, *Nature*, 2024, **635**, 874–881.
29 T. Meier, H. Bässler and A. Köhler, *Advanced Optical Materials*, 2021, **9**, 2100115.
30 J. Li, H. Zhang, S. Wang, D. Long, M. Li, D. Wang and T. Zhang, *Materials*, 2018, **11**, 717.
31 W. Xu, T. Du, M. Sachs, T. J. Macdonald, G. Min, L. Mohan, K. Stewart, C.-T. Lin, J. Wu, R. Pacalaj, S. A. Haque, M. A. McLachlan and J. R. Durrant, *Cell Reports Physical Science*, 2022, **3**, 100890.
32 A. B. Andrabi and A. T. Mallajosyula, *Solar Energy*, 2023, **264**, 112020.
33 J. Pan, Z. Chen, T. Zhang, B. Hu, H. Ning, Z. Meng, Z. Su, D. Nodari, W. Xu, G. Min, M. Chen, X. Liu, N. Gasparini, S. A. Haque, P. R. F. Barnes, F. Gao and A. A. Bakulin, *Nature Communications*, 2023, **14**, 8000.
34 M. Shekarnoush, L. Fernandez-Izquierdo, F. S. Aguirre-Tostado, Z. H. Shamsi and M. A. Quevedo-Lopez, *Chem. Mater.*, DOI:10.1021/acs.chemmater.3c01440.
35 R. Wayne, Image J (version 1.54p) National Institutes of Health and the Laboratory for Optical and Computational Instrumentation 2025.

View Article Online
DOI: 10.1039/D6MA00161K

The data supporting this article have been included as part of the Supplementary Information. Supplementary information: Figure S1, Tables S1, Section S1, Figure S2, Figure S3, Figure S4, Table S2, Figure S5, Section S2, Section S3 and Figure S6. Further data supporting the findings of this study are available from the corresponding author upon reasonable request.